Ejigu, Yohannes Getachew; Boy, Jean-Paul; Raja-Halli, Arttu; Khorrami, Fatemeh; Näränen, Jyri; Nordman, Maaria

Analyzing the 3D Deformation Induced by Non-tidal Loading in GNSS Time Series in Finland

Published in:
International Association of Geodesy Symposia

DOI:
10.1007/1345_2024_259

E-pub ahead of print: 11/07/2024

Document Version
Publisher's PDF, also known as Version of record

Analyzing the 3D Deformation Induced by Non-tidal Loading in GNSS Time Series in Finland

Yohannes Getachew Ejigu, Jean-Paul Boy, Arttu Raja-Halli, Fatemeh Khorrami, Jyri Naranen, and Maaria Nordman

Abstract

Improving our understanding of non-tidal loading (NTL) in geodetic time series, especially at regional and local scales, holds paramount importance. This deeper comprehension enables accurate modeling and effective removal of NTL effects from the time series, consequently enhancing the overall stability and reliability of geodetic observations. In this study, we compared the performance of different loading products and investigated their impact on the 20-year time series of four permanent GNSS stations within the Finnish permanent GNSS network (FinnRef). We employed original GNSS time series data products generated by four different analysing centers. We qualitatively compared NTL corrections involving ten different combinations of different hydrological, non-tidal atmospheric, and non-tidal oceanic loading models to see how various loading configurations operate and how they affect the noise characteristics of GNSS 3D time series, and ultimately to figure out which models are the most realistic in Finland. We observed weighted RMS reduction rates of up to 20% for the vertical coordinate and up to 10% for the horizontal coordinate. Additionally, we identified a maximum annual amplitude reduction rate of 87.2%. The results demonstrate a substantial improvement through the integration of hydrological loading products derived from GRACE satellites in our study conducted over Finland.

Keywords

Annual amplitude and phase · GNSS time series · Non-tidal loading · RMS reduction rate · Trend and trend uncertainty

1 Introduction

At different scales in space and time, the Earth's surface is subject to various perturbations, including tectonic movements, volcanic eruptions, and landslides. Mass changes in oceans, atmosphere, groundwater, and other natural systems induce detectable changes in the Earth's shape and gravity field (Blewitt et al. 2001). Responding to mass redistribution occurring on sub-daily to inter-annual timescales, which are not due to gravitational forces from Sun and Moon, is referred to as non-tidal loading (NTL). In theory, over seasonal timescales, non-tidal atmospheric, and hydrological loading have the potential to induce deformations of up to

Y. G. Ejigu (✉) · F. Khorrami
Department of Built Environment, School of Engineering, Aalto University, Espoo, Finland
e-mail: yohannesgetachew.ejigu@aalto.fi

J.-P. Boy
Institut Terre and Environnement de Strasbourg, University de Strasbourg, CNRS UMR7063, Strasbourg, France

A. Raja-Halli · J. Naranen
Finnish Geospatial Research Institute, National Land Survey, Espoo, Finland

M. Nordman
Department of Built Environment, School of Engineering, Aalto University, Espoo, Finland

Finnish Geospatial Research Institute, National Land Survey, Espoo, Finland

International Association of Geodesy Symposia,
https://doi.org/10.1007/1345_2024_259,

30 mm in the vertical coordinate (van Dam et al. 2001; Schuh et al. 2003).

Global Navigation Satellite Systems (GNSS) have been used to explore geophysical phenomena, including the NTL surface deformation (e.g., Nordman et al. 2009, 2015, van Dam et al. 2012, Mémin et al. 2020. GNSS position time series often exhibit unforeseen broadband fluctuations (such as a nonlinear motion) depending on unknown deterministic parameters (Bevis and Brown 2014), and unknown stochastic parameters (Bos et al. 2020), characterized by power-law and white noise models (Mao et al. 1999; Williams et al. 2004; Santamaria-Gomez et al. 2011). Interpreting interannual variations in GNSS position time series and their common modes across a region remains a challenging task due to the correlation between NTL and noise variations (Williams et al. 2004). Moreover, GNSS serves as a pivotal geodetic technique, providing essential input to the International Terrestrial Reference Frame (ITRF) for the precise computation of coordinates (Altamimi et al. 2016). Correcting the NTL could contribute to the stability of the ITRF by improving the GNSS positioning quality, and statistical modelling of geodetic time series.

The NTL typically encompasses non-tidal atmospheric loading (NTAL), non-tidal ocean loading (NTOL), and hydrological loading (HYDL). In their recent study, Nicolas et al. (2021) showed the impact of river storage-induced HYDL on the substantial enhancement of both vertical and horizontal GNSS displacements in regions across South America. Klos et al. (2021) found that HYDL contributes to GNSS displacements within the seasonal band, while NTAL exhibits a positive correlation with GPS displacements across a range of temporal resolutions. Li et al. (2020) conducted a comparative analysis of surface mass loading corrections in GNSS time series, with a reduction in the RMS value reaching up to 20% in the vertical component. Nordman et al. (2009) employed tide gauge data to assess the impact of NTOL on the vertical positioning of GPS stations in the Baltic Sea. Overall, numerous researchers have delved into the deformation resulting from NTL. However, the majority of these studies focus on the separation of NTL into distinct components such as NTAL (e.g., Tregoning and van Dam 2005; Tregoning and Watson 2011), NTOL (e.g, Nordman et al. 2009; van Dam et al. 2012; Geng et al. 2012; Williams and Penna 2011, Gobron et al. 2021), and HYDL (van Dam et al. 2001, 2007; Davis et al. 2004; Tregoning et al. 2009). This study, however, is focused on examining the combined contributions of NTAL, NTOL, and HYDL in long-period GNSS time series data.

The NTL displacement products are available from different Earth System Modeling groups, including the School and Observatory of Earth Sciences (EOST)[1] loading service from the University of Strasbourg, and the German Research Center for Geosciences in Potsdam (ESMGFZ).[2] We conducted a comprehensive performance comparison of the EOST and ESMGFZ loading model products while also examining their influence on the scatter of GNSS time series data across four permanent GNSS stations of the FinnRef network. Furthermore, we delved into different loading configurations and their respective impacts on the noise characteristics of GNSS vertical displacement trend time series. Ultimately, our objective is to identify the most optimal loading models within the context of the Finnish region.

In this chapter, we first present a concise overview of the GNSS processing strategy and introduce the NTL computation, including the use of different models (Sect. 2). Section 3 presents results obtained before and after implementing NTL corrections. The chapter concludes in Sect. 4 with a summary of findings and an outlook for future research.

2 Data and Methods

2.1 GNSS Data and Processing

In this study, we focused on four GNSS stations within the FinnRef network in Northern Europe: JOEN in East Finland, METS in South Finland, SODA in North Finland, and VAAS in West Finland (for locations, see Fig. 3). Our analysis encompassed a 20-year (2002–2022) dataset obtained from three distinct GNSS analysis centers including the Nevada Geodetic Laboratory (NGL, Blewitt et al. 2018), the Jet Propulsion Laboratory (JPL, specifically 'JPL-2018a', Bertiger et al. 2020), and the IGS CNES-CLS analysis center (hereafter referred to as CNE, Michel et al. 2021). Furthermore, we created our own solution, processing GNSS data using PRIDE-AR ver 2.2 GNSS software (Geng et al. 2019a). Both NGL and JPL position timeseries products were estimated using the JPL GipsyX software, while CNES utilized the GINS software.

In both NGL and PRIDE (PRI), the apriori tropospheric delays are sourced from the Vienna Mapping Function (VMF1) grids (Böhm et al. 2006b). Also, the hydrostatic and wet zenith delays are mapped to observation elevations using VMF1. The JPL and CNE solutions employ the global mapping function (GMF) (Böhm et al. 2006a) for tropospheric modeling, along with the global pressure and temperature empirical function GPT2 (Lagler et al. 2013) to estimate tropospheric delays.

All four GNSS (actually GPS-only) datasets share a common processing strategy based on precise point positioning (PPP) (Zumberge et al. 1997) with carrier phase ambiguity resolution (JPL and NGL (Bertige et al. 2010), CNE (Loyer et al. 2012) and PRI (Geng et al. 2019b)). The final

[1] http://loading.u-strasbg.fr/.

[2] http://rz-vm115.gfz-potsdam.de:8080/repository.

daily coordinates position time series are expressed in the IGS14 reference frame (Altamimi et al. 2016). The impact of the first-order ionospheric effect was removed using the ionospheric-free linear combination. A second-order calibration of the remaining ionosphere effects was implemented using IGS's global ionospheric maps in conjunction with the International Geomagnetic Reference Field (IGRF-12)'s magnetic field model; the solid Earth tide and pole tide were corrected according to the IERS 2010 Conventions, and the ocean tide loading effect were corrected using the FES2004 model (Lyard et al. 2006). The NTL corrections were not applied to these timeseries products. The resulting time series are in CF frame at non-secular time scale (Dong et al. 2003).

2.2 Non-tidal Loading Time Series Data

We used NTL-induced surface deformation timeseries from two Earth System Modeling groups: EOST and ESMGFZ Loading Service. Both modeling groups employ Green's functions to calculate NTL displacements; however, they employ slightly different procedures for computing the integrals. The EOST group utilizes the rheological parameters from the PREM (Preliminary Reference Earth Model, Dziewonski and Anderson 1981) Earth model to compute displacement, whereas the GFZ employs the Elastic Earth model "ak135" (Kennett et al. 1995) for their calculations. In both EOST and GFZ products, we averaged time series into daily time series to harmonize their temporal resolutions. In this study, the NTL products utilized are in CF, and the summary including their providers is shown in Table 1.

Table 1 Loading products provided by EOST and GFZ. The different abbreviations in the loading source and models columns refer to different products and data centers providing the data

Dataset/Load	Models	Spatial/Temporal Res.
EOST/NTAL	ERA5/IB	0.25° × 0.25°/1 h
	ERA5/TUGO-m[a]	0.25° × 0.25°/1 h
	ECMWF OP/IB	0.5° × 0.5°/3 h
	MERRA2/IB	0.5° × 0.5°/1 h
GFZ/NTAL	ECMWF OP	0.5° × 0.5°/3 h
EOST/NTOL	ECCO2	0.25° × 0.25°/24 h
GFZ/NTOL	MPIOM	1° × 1°/3 h
EOST/HYDL	ERA5	0.25° × 0.25°/1 h
	GLDAS2/Noah	0.5° × 0.5°/3 h
	MERRA2	0.50 × 0.625°/1 h
	GRACE[a, b]	1° × 1°/monthly
GFZ/HYDL	LSDM	0.5° × 0.5°/24 h
NASA/HYDL[c]	GRACE/GSFC/Mascons[b]	1° × 1°/monthly

For more detailed explanations see websites of EOST[1] and ESMGFZ[2]
[a]TUGO-m model is the sum of NTAL and NTOL circulation model (such as ECCO2) [1]. EOST GRACE is the sum of HYDL and NTOL[1]
[b]We used GRACE-derived data provided by EOST and NASA (Argus et al. 2022). For more details, see websites[1,3]
[c]https://grace.jpl.nasa.gov/data/get-data/jpl_global_mascons/

3 Results and Discussion

3.1 Optimal Fusion of NTL

We undertake a comprehensive quantitative evaluation to assess the cumulative impact resulting from three distinct categories of NTL-induced displacements, namely NTAL, NTOL, and HYDL. Consequently, we establish a total of eight combinations within the EOST category and the two combinations within GFZ. The summary of these combinations can be found in Table 2.

Moreover, we applied these NTL correction combinations to our four original (reference) time series for the four stations under study without interpolating any gaps.

In general, we observed a reduction in the scattering of the original displacement time series (not shown here) after applying the correction. The RMS scatter exhibits improvement, with RMS difference between the original and corrected RMS scatter ranging from −0.93 mm to 4.5 mm, positive numbers meaning reduction in the scatter and negative numbers meaning increase in the scatter. The extent of this improvement varies based on the specific station and the type of NTL correction combination implemented. For the up component, the RMS differences between the original and corrected RMS scatter range from −0.93 mm to 3.51 mm for JPL time series, −0.71 mm to 2.73 mm for CNE time series, −0.73 mm to 2.85 mm for NGL time series, and − 0.72 mm to 4.52 mm for PRI time series, as shown in Fig. 1 (third column). The RMS difference in the horizontal components is minimal, with a positive deviation of up to +0.5 mm in the east and a negative deviation of up to −0.5 mm in the north (Fig. 1, first and second columns).

A comprehensive overview and assessment of the effectiveness of various environmental loading products were obtained through a computation of the weighted RMS (WRMS) percentage reduction rates between the original GNSS position time series and the combined NTL corrected time series. The WRMS was computed as,

Table 2 Combinations of NTL correction

	Combination
EOST1	ERA5IB + ECCO2 + ERA5hyd
EOST2	ERA5TUGO + ERA5hyd
EOST3	ECMWF-OP/IB + ECCO2 + ERA5hyd
EOST4	MERRA2 + ECCO2 + GLDAS
EOST5	MERRA2 + ECCO2 + MERRA2h
EOST6	ERA5IB + GRACE
EOST7	MERRA2IB + GRACE
EOST8	MERRA2IB + ECCO2 + GRACE NASA mascon
GFZ1	GFZ NTAL + GFZ NTOL + GFZ HYDL
GFZ2	GFZ NTAL + GFZ NTOL + GRACE NASA mascon

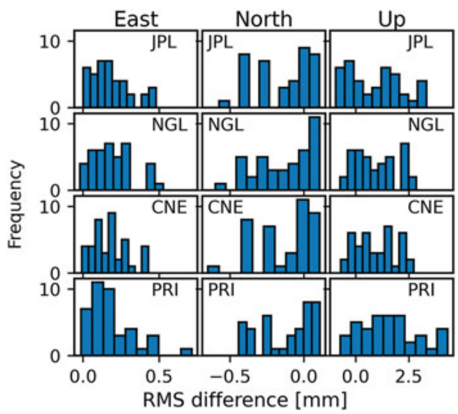

Fig. 1 RMS difference between the original and ten NTL corrected time series for four stations. The y-axis frequency refers to the data from these four stations multiplied by the ten different NTL corrections

$WRMS = \sqrt{\frac{1}{N-1}\sum_{i=1}^{N}\left(\frac{(Ts_i-\overline{Ts_i})^2}{\sigma_i^2}\right)/\sum_{i=1}^{N}\sigma_i^2}$, where Ts_i is the daily coordinate displacement solution, N is the number of data points of Ts_i, and σ_i is the standard deviation (formal error) of Ts_i. However, we merely considered the formal error information from the GNSS time series solution and did not include the NTL formal error information. The weighted average value, Ts_i, was calculated as, $\overline{Ts_i} = \sum_{i=1}^{N}\left(\frac{Ts_i}{\sigma_i^2}\right)/\sum_{i}^{N}\frac{1}{\sigma_i^2}$. The WRMS percentage reduction rate is given by, $Red_{WRMS} = (1 - WRMS_c/WRMS_o) \times 100\%$, where $WRMS_o$ and $WRMS_c$ refer to the original and NTL corrected WRMS, respectively.

As an example, Fig. 2 shows WRMS percentage reduction rates for both the horizontal (East and North) and vertical (Up) coordinate time series at station METS. The RMS reduction rates in all three coordinate time series exhibited positive values for all solutions, with considerable variation depending on the GNSS solution products and stations. Maximum reductions reached approximately 10% in the horizontal direction and about 20% in the vertical direction. In all NTL corrections, both the JPL solution and our PRI solution consistently demonstrate substantial reductions. In respect to combinations of NTL correction, we observed high reductions between the original data and the corrections applied in EOST7 and EOST8 across all solution products and stations compared to other corrections. It's important to note that our EOST7 and EOST8 corrections incorporate the HYDL obtained from GRACE. This aligns with the findings of Springer et al. (2019), who showed that HYDL-induced deformation obtained from GRACE can explain up to 25% of the deformation in daily GNSS height time series in Southeastern Europe. On the other hand, the corrections from EOST showed consistently higher RMS reduction rates in all solution products and stations when compared to those obtained from GFZ. Specifically, the correction derived from the internal combination at GFZ, referred to as GFZ1, exhibited the lowest reduction in RMS error. This again demonstrates that the GRACE hydrological loading significantly contributes to reducing the RMS error in NTL corrections. In prior research, Nordman et al. (2015) noted a maximum 16% reduction in variance in the vertical coordinate for inter-station vectors among GNSS stations in the Baltic Sea, specifically for NTOL corrections during the period from 2008 to 2012.

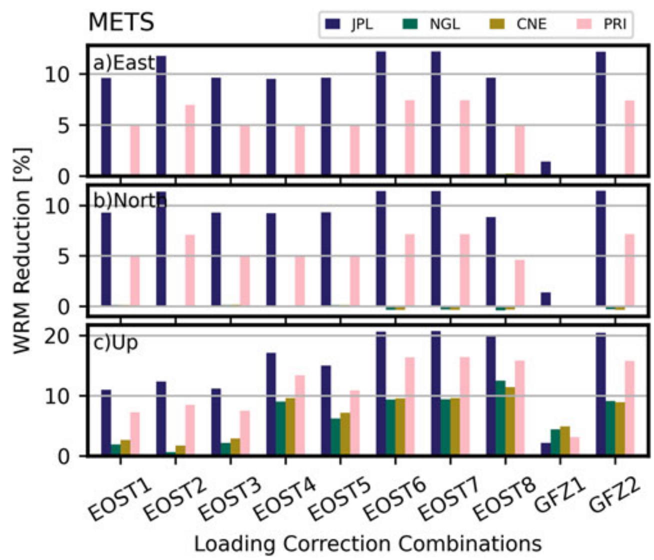

Fig. 2 Percentage reduction of WRMS for 3D deformation (East-North-Up from top to bottom) with NTL corrections applied at station METS, for the period from 2002 to 2022

3.2 Annual Signal and Frequency Content

To understand the time series behaviour better, we analyzed the spectral characteristics, including annual amplitude, phase, and trends, of GNSS coordinate time series both in their original form and after applying corrections, using Hector software version 1.9 (Bos et al. 2021). During the estimation of these parameters in Hector, the noise combination of power-law and white noise (PL + WN) model was utilized in the analysis of stochastics characteristic of GNSS coordinate time series. This noise model was applied to the residual time series and allowed for the simultaneous estimation of the non-integer spectral index of the residual series.

Figure 3 illustrates a comparison between the annual amplitude and phase changes for the vertical component, highlighting notable discrepancies in the annual signal amplitudes across various stations. We found that the peak annual amplitude and phase of the considered stations generally occur between July and October, except for the West Finland station (VAAS), where the maximum annual amplitude and phase extend from January to April. Upon applying corrections, the annual amplitude decreased in

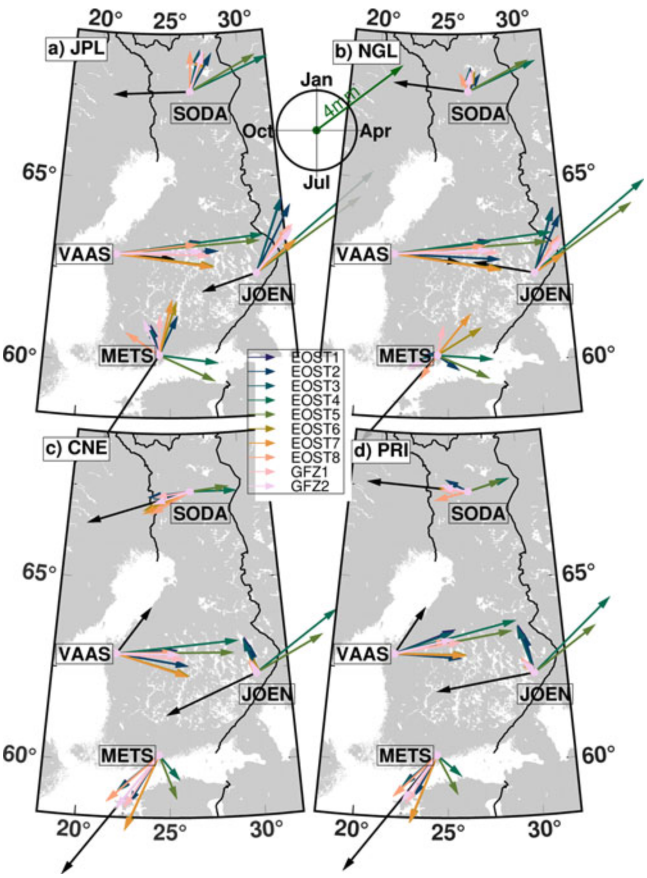

Fig. 3 Comparison of amplitude and phase maps for the vertical component annual signals between the Original GNSS time series (black) and results with NTL corrections (other colours) at four selected stations. The annual amplitude is represented by the length of the arrows. The direction of each arrow indicates the peak-value month, measured in a clockwise direction from the North, starting with January

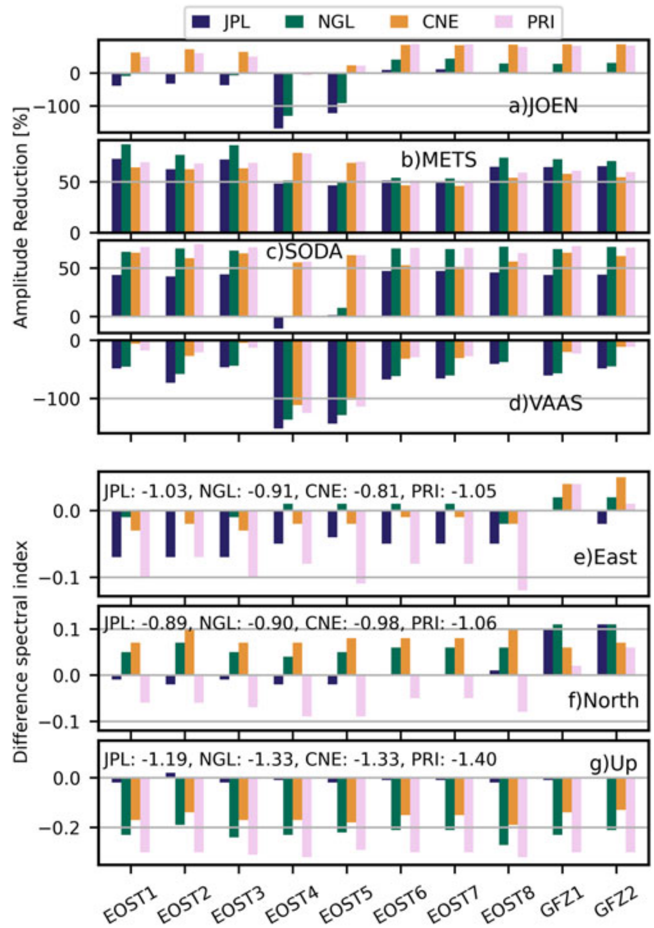

Fig. 4 (**a–d**) Percentage reduction in spectral annual amplitude for Up component deformation with NTL corrections applied at stations JOEN, METS, SODA and VAAS, and (**e–g**) the spectral index difference (original minus corrected) for 3D deformation (East-North-Up from top to bottom). The number in (**e–f**) panel shows the spectral index estimated from the original time-series

all combinations for stations METS and SODA, and in combinations EOST 4-8, as well as GFZ1-2 for station JOEN. Both the JPL and NGL series display a out-of-phase variation in the annual phases for three of the considered stations (JOEN, METS, and SODA). In contrast, the CNE and PRI series consistently maintain the annual phase pattern across the four GNSS series. Notably, at station METS, the annual signal phase of the JPL and NGL series diverges by 90 to 180° (typically equivalent to 091 to 182 days of year) from the original signal's annual phase, pointing in different directions.

To statistically evaluate the impact of NTL corrections on the annual signal, we also employ the amplitude reduction rate, $Red_{Amp} = (1 - Amp_c/Amp_o) \times 100\%$, where Amp_o and Amp_c refers to the orginal and NTL corrected annual amplitudes, respectively. As depicted in Fig. 4 (a–d), the amplitude generally decreases after applying the correction for most NTL corrections. However, there are exceptions, such as in the case of station JOEN, where some corrections, and station VAAS where almost all corrections result in a negative reduction (meaning the amplitude is increased). The maximum reduction rate observed is 87.2% for the PRI solution in relation to the EOST6 and EOST7 corrections. For METS, the minimum annual amplitude reduction rate is 46.6% observed for the EOST5 correction in the JPL solution, while the maximum reduction rate reaches 86.7% for the EOST1 correction in the NGL solution. Regarding SODA, overall observe positive reduction rates were observed, except for the EOST4 correction in the JPL solution. The highest reduction rate, reaching 74.4%, is seen in the PRI solution. However, for VAAS, we found negative reduction rates, with the maximum reduction rate being −1.4% for the EOST7 and EOST8 corrections in the CNE and PRI solutions.

The presence of noise in the GNSS coordinate time series can have a substantial impact on the accuracy and induced error in the geodetic time series of the annual signal (Blewitt et al. 2001; Collilieux et al. 2007). To examine the effect of NTL deformation in the GNSS time series on the annual signal, we computed the average Lomb-Scargle periodogram of the coordinate residuals before and after applying NTL corrections. Figure 4 (e–g) depicts the difference in the stacked median estimated spectral index of the PL + WN noise model between its original and corrected. We observed a significant reduction in the spectral index for PRI solutions in the East (−1.05 to −0.93), North (−1.06 to −0.97) and Up (decreasing from −1.4 to −1.08) after correction. Particularly noteworthy was the consistent reduction in the spectral index for the North component exclusively in PRI solutions across all EOST corrections. Additionally, notable reductions were observed for NGL and CNE solutions in the East and Up components. In contrast, corrections did not affect the spectral index in the JPL solution, resulting in contrasting outcomes in WRMS comparisons. This indicates that the WRMS reduction is due to the high portion of white noise in the time series. The exemplary stacked median spectral density (PSD) estimated for vertical coordinate residuals time series for the CNE solution is shown in Fig. 5. In the PSD, it can be observed that the annual peak of the time series is weakened to some extent after the correction for NTL. However, it is important to note that the NTL corrections do not completely eliminate the annual peaks. Nevertheless, there is a large reduction in frequency bands in the annual and between roughly 3–6 months, particularly noticeable in EOST7, EOST8, and in both GFZ1 and GFZ2 corrections. This would agree with Klos et al. (2021), who showed that the frequency bands of annual and between 4–9 months exhibit notable significant RMS reductions (>40%) after correcting for HYDL. This suggests a robust sensitivity to hydrological variations, elucidating a substantial portion of the seasonal signals in GNSS displacements.

To analyze the effect of NTL correction on the trend (velocity) and trend uncertainty in our regional stations, we conducted further assessments. The up-coordinate trends observed for the stations under consideration, JOEN, METS, SODA, and VAAS, fall within the ranges of 3.44–3.93 mm/year, 4.06–4.63 mm/year, 7.13–7.69 mm/year, and 9.18–9.89 mm/year, respectively. To illustrate this, we present the statistical results after correction for the up-coordinate trend and trend uncertainty for station JOEN in Fig. 6. It is evident that after applying the loading correction, the overall trend shows a decrease, with the exception of the EOST1, EOST2, EOST3 and GFZ1 corrections. For the EOST6, EOST7, EOST8, and GFZ2 corrections, the effect on trend values can decrease by up to 0.6 mm/year for the NGL solution and 0.4 mm/year for the other three solutions compared to the original solution trend (see Fig. 6). Similar results were observed for other stations, although they are not

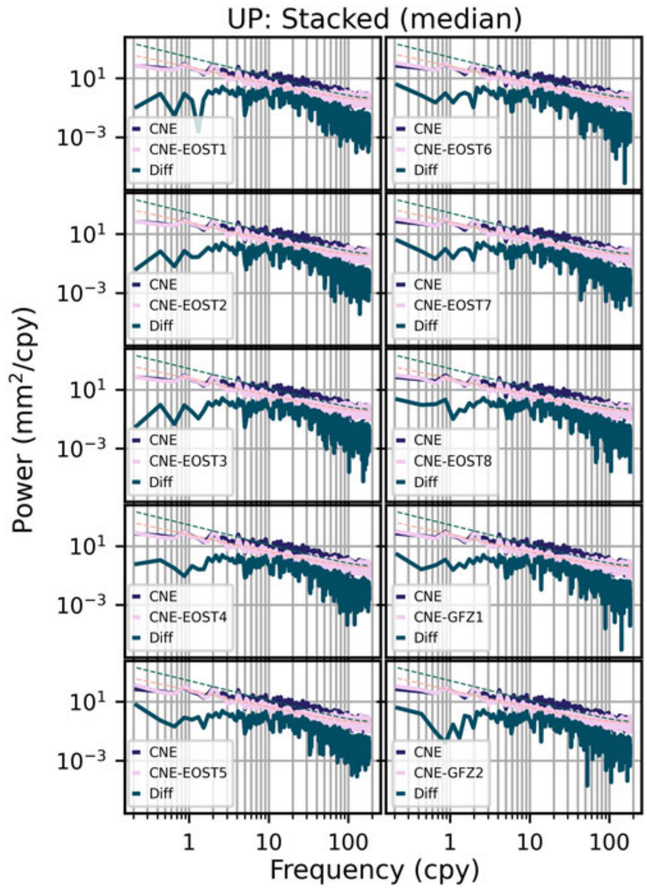

Fig. 5 Stacked power spectral densities (PSDs) plotted for vertical component of CNE solution. The original GNSS displacements are represented in blue, the NTL-corrected displacements are illustrated in pink, and the differences are highlighted in green. The dashed green and red lines indicate the estimated PL + WN noise model for the original and corrected displacements, respectively

shown here. This result is in line with the study of Gobron et al. (2021), who demonstrated that trend uncertainties were reduced by 70% at high latitudes after applying combinations of NTAL and NTOL correction in up-displacements.

In general, when comparing different NTL correction combinations, EOST1-3 seem to produce smallest improvements. The NTAL corrections for these three combinations are from ERA5, whereas other models are used for other combinations. Integrating HYDL data of GLDAS and MERRA2h in EOST4 and EOST5 improves WRMS reduction rates, while impacts on annual amplitude vary by station. Notable differences between EOST6 and EOST7 are in their NTAL components (ERA5IB and MERRA2IB), with EOST7 showing significant enhancements. Difference in HYDL components between GFZ1 and GFZ2 are the ESMGFZ hydrology model and GRACE product, respectively. Overall, GFZ2, EOST7 and EOST8 results that have GRACE-derived HYDL, outperform others.

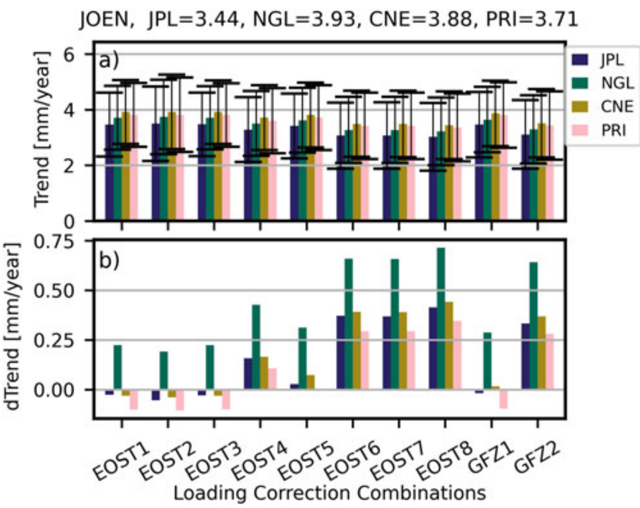

Fig. 6 Trend and uncertainties after NTL Correction for JOEN. (**a**) the trend of the over 20-year time series. (**b**) the difference in trend before and after NTL correction. The error bars in the top panel represent the uncertainty in the trend estimation. The numbers on top of the top panel header denote the trends in the original time series in mm/year

4 Conclusions and Outlook

We compared NTL corrections for four GNSS stations in Finland, using data from our PPP PRIDE GNSS processing and three other centers. While processing strategies were similar, a key difference was found in the tropospheric delay model and mapping functions.

The WRMS reduction in GNSS time series varies with different combinations of NTL products. Variations in reduction rates underscore the importance of selecting appropriate GNSS solution products and considering station characteristics. Stations like SODA, JOEN, and VAAS demonstrate diverse behaviors. Both JPL and PRI solutions consistently achieve substantial WRMS reductions across various NTL correction combinations, indicating their reliability. Differences between EOST and GFZ corrections highlight the importance of careful model selection for GNSS processing. The qualitative comparison of various combinations of NTL corrections, notably, the combinations involving EOST7 and EOST8 NTL corrections exhibited significant reductions in WRMS compared to other combinations.

Our analysis revealed a general decrease in amplitudes, spectral index, trend (velocity) and trend uncertainity after NTL corrections. Some corrections even led to negative reduction rates for the annual amplitude (i.e., increase). In most of the considered stations, annual amplitude reduction rates of the solution product were positive, indicating that the corrections tended to reduce the amplitude of the data, potentially improving data accuracy. After applying corrections, particularly in the case of JPL and NGL data, noticeable out-of-phase variations in annual phases were observed at some stations, while the spectral index generally exhibited a decreasing in the annual peak. In contrast, CNE and PRI data consistently preserved the annual phase pattern across all stations.

Integrating GLDAS and MERRA2h data from HYDL improves WRMS reduction rates, while the extent of improvement in the annual amplitude reduction rate varies from station to station. This suggests that the inclusion of these datasets exhibits different characteristics depending on the local stations. The GRACE-dervied HYDL notably reduces RMS error, annual amplitude, trend and trend uncertainties in EOST7, EOST8, and GFZ2, emphasizing the importance of dedicated gravity missions like GRACE and GRACE-FO in improving GNSS corrections. Further analysis is needed to refine correction methods and enhance data accuracy for regional and local geodetic stations.

Acknowledgements The authors would like to express their gratitude to JPL, NGL, and CNES for GNSS coordinate data, as well as to GFZ, EOST, and NASA for loading model data publicly available. We are also grateful to the two anonymous reviewers for their constructive suggestions during the review of this manuscript.

References

Altamimi Z, Rebischung P, Metivier L, Collilieux X (2016) ITRF2014: a new release of the international terrestrial reference frame modeling nonlinear station motions. J Geophys Res Solid Earth 121(8):6109–6131

Argus DF, Martens HR, Borsa AA, Knappe E, Wiese DN, Alam S, Gardiner WP (2022) Subsurface water flux in California's Central Valley and its source watershed from space geodesy. GRL 49(22)

Bertige W, Desai SD, Haines B, Harvey N, Moore AW, Owen S, Weiss JP (2010) Single receiver phase ambiguity resolution with GPS data. J Geod 84:327–337

Bertiger W, Bar-Sever Y, Dorsey A et al (2020) Gipsyx/rtgx, a new tool set for space geodetic operations and research. Adv Space Res 66(3):469–489

Bevis M, Brown A (2014) Trajectory models and reference frames for crustal motion geodesy. J Geod 88:283–311

Blewitt G, Lavalle D, Clarke P et al (2001) A new global mode of earth deformation: seasonal cycle detected. Science 294(5550):2342–2345

Blewitt G, Hammond W et al (2018) Harnessing the GPS data explosion for interdisciplinary science. Eos 99

Böhm J, Niell A, Tregoning P et al (2006a) Global mapping function (GMF): a new empirical mapping function based on numerical weather model data. Geophys Res Lett 33(7)

Böhm J, Werl B, Schuh H (2006b) Troposphere mapping functions for GPS and very long baseline interferometry from european Centre for medium-range weather forecasts operational analysis data. J Geophs Res: solid earth 111(B2)

Bos MS, Montillet JP, Williams SD et al (2020) Introduction to geodetic time series analysis. Geodetic Time Series Analysis Earth Sci:29–52

Bos M, Fernandes R, Bastos L (2021) Hector user manual version 1.9. Tech. Rep., tech. Rep. SEGAL Universidade da Beira Interior, Covilha

Collilieux X, Altamimi Z, Coulot D, Ray J, Sillard P (2007) Comparison of very long baseline interferometry, GPS, and satellite laser ranging height residuals from ITRF2005 using spectral and correlation methods. J Geophys Res Solid Earth 112(B12)

Davis JL, Elosegui P, Mitrovica JX, Tamisiea ME (2004) Climate driven deformation of the solid earth from GRACE and GPS. Geophys Res Lett

Dong D, Yunck T, Heflin M (2003) Origin of the international terrestrial reference frame. J Geophys Res Solid Earth 108(B4)

Dziewonski AM, Anderson DL (1981) Preliminary reference Earth model. Physics of the earth and planetary interiors. 25(4):297–356.

Geng J, Williams SDP, Teferle FN, Dodson AH (2012) Detecting storm surge loading deformations around the southern North Sea using subdaily GPS. Geophys J Int 191(2):569–578

Geng J, Chen X, Pan Y et al (2019a) PRIDE PPP-AR: an open-source software for GNSS PPP ambiguity resolution. GPS Solutions 23:1–10

Geng J, Chen X, Pan Y, Zhao Q (2019b) A modified phase clock/bias model to improve PPP ambiguity resolution at Wuhan University. J Geod 93(10):2053–2067

Gobron K, Rebischung P, Van Camp M, Demoulin A, de Viron O (2021) Influence of aperiodic non-tidal atmospheric and oceanic loading deformations on the stochastic properties of global GNSS vertical land motion time series. J Geophys Res Solid Earth 126:e2021JB022370

Kennett BL, Engdahl ER, Buland R (1995) Constraints on seismic velocities in the Earth from traveltimes. Geophys J Int 122(1):108–124

Klos A, Dobslaw H, Dill R et al (2021) Identifying the sensitivity of GPS to non-tidal loadings at various time resolutions: examining vertical displacements from continental eurasia. GPS Solutions 25(3):89

Lagler K, Schindelegger M, Bohm J et al (2013) GPT2: Empirical slant delay model for radio space geodetic techniques. Geophys Res Lett 40(6):1069–1073

Li C, Huang S, Chen Q et al (2020) Quantitative evaluation of environmental loading induced displacement products for correcting GNSS time series in cmonoc. Remote Sens 12(4):594

Loyer S, Perosanz F, Mercier F, Capdeville H, Marty JC (2012) Zero-difference GPS ambiguity resolution at CNES–CLS IGS analysis center. J Geod 86:991–1003

Lyard F, Lefevre F, Letellier T. et al (2006) Modelling the global ocean tides: modern insights from FES2004. Ocean Dynamics 56:394–415. https://doi.org/10.1007/s10236-006-0086-x

Mao A, Harrison CG, Dixon TH (1999) Noise in GPS coordinate time series. J Geophy Res Solid Earth 104(B2):2797–2816

Mémin A, Boy JP, Santamaria-Gomez A (2020) Correcting GPS measurements for non-tidal loading. GPS Solutions 24:1–13

Michel A, Santamaria-Gomez A, Boy JP et al (2021) Analysis of gnss displacements in europe and their comparison with hydrological loading models. Remote Sens 13(22):4523

Nicolas J, Verdun J, Boy JP et al (2021) Improved hydrological loading models in South America: analysis of gps displacements using m-ssa. Remote Sens 13(9):1605

Nordman M, Makinen J, Virtanen H et al (2009) Crustal loading in vertical GPS time series in fennoscandia. J Geodyn 48(3–5):144–150

Nordman M, Virtanen H, Nyberg S et al (2015) Non-tidal loading by the Baltic Sea: comparison of modelled deformation with GNSS time series. Geo Res J 7:14–21

Santamaria-Gomez A, Bouin MN, Collilieux X et al (2011) Correlated errors in gps position time series: implications for velocity estimates. J Geophy Res Solid Earth 116(B1)

Schuh H, Estermann G, Cretaux JF, Berge-Nguyen M, van Dam T (2003) Investigation of hydrological and atmospheric loading by space geodetic techniques. In: C Hwang, CK Shum, JC Li (eds) IAG Proceedings, vol 126, pp 123–132

Springer A, Karegar MA, Kusche J, Keune J, Kurtz W, Kollet S (2019) Evidence of daily hydrological loading in GPS time series over Europe. J Geod 93:2145–2153

Tregoning P, van Dam TM (2005) Atmospheric pressure loading corrections applied to GPS data at the observation level. Geophys Res Lett

Tregoning P, Watson C (2011) Correction to "atmospheric effects and spurious signals in GPS analyses". J Geophys Res

Tregoning P, Watson C, Ramillien G, McQueen H, Zhang J (2009) Detecting hydrologic deformation using GRACE and GPS. Geophys Res Lett

van Dam T, Wahr J, Milly PCD, Shmakin AB, Lavalle BD, Larson KM (2001) Crustal displacements due to continental water loading. Geophys Res Lett 28(4):651–654

van Dam T, Wahr J, Lavallée D (2007) A comparison of annual vertical crustal displacements from GPS and Gravity Recovery and Climate Experiment (GRACE) over Europe. J Geophys Res 112:B03404. doi:10.1029/2006JB004335.

van Dam TM, Collilieux X, Altamimi Z, Ray J (2012) Non-Tidal Ocean loading: amplitudes and potential effects in GPS height time series. J Geod 86(11):1043–1057

Williams SDP, Penna NT (2011) Non-Tidal Ocean loading effects on geodetic GPS heights. Geophys Res Lett

Williams SD, Bock Y, Fang P, Jamason P, Nikolaidis RM, Prawirodirdjo L, Miller M, Johnson DJ (2004) Error analysis ofcontinuous GPS position time series. J Geophys Res Solid Earth 109(B3)

Zumberge J, Heflin M, Jefferson D et al (1997) Precise point positioning for the efficient and robust analysis of GPS data from large networks. J Geophys Res Solid Earth 102(B3):5005–5017